Cherenkov Maser Amplifier

Paul Argyle[®], Member, IEEE, and Phillip Sprangle, Life Fellow, IEEE

Abstract—A Cherenkov maser amplifier (CMA) for generating high-power levels over a wide frequency range is proposed, analyzed, and numerically simulated. The CMA is a wideband amplifier consisting of an annular relativistic electron beam in a cylindrical waveguide, having an inner conductor and outer layer of dielectric material all enclosed by an outer conductor. The interaction between the hybrid TEM/TM subluminal mode of the waveguide and the relativistic electron beam leads to amplification over a wide range of input frequencies in the gigahertz regime. The interaction is analyzed and simulated in the linear and nonlinear regimes. We show that conversion efficiencies can be enhanced by spatially tapering the dielectric waveguide. In addition, by premodulating the electron beam, efficiencies can be further enhanced and saturation distances reduced. Conversion efficiencies greater than 25% have been simulated by premodulating the electron beam and/or spatially tapering the dielectric waveguide over distances of a few meters. Simulation examples indicate that the ultrawideband CMA configuration operating in the gigahertz regime can generate power levels in the gigawatt range, employing electron beams in the multi-kiloampere and low megaelectronvolt range.

 ${\it Index Terms} \hbox{---} {\it Cherenkov maser, dielectric, wideband amplifiers.}$

I. INTRODUCTION

Compact, high-power, and wideband amplifiers, operating in the gigahertz frequency regime, have important applications, ranging from RF communications with ground and airborne systems to electronic disruption. To achieve the necessary waveform diversity and agility, high-power amplifiers are needed for these applications.

This article presents an amplification mechanism capable of amplifying very wideband radiation in the gigahertz regime, at power levels in the gigawatt range using the present-day technology. We propose a Cherenkov maser amplifier (CMA) in which a high-current, relativistic electron beam is injected and propagates in a dielectrically lined waveguide [1]. The CMA analyzed and simulated in this article differs from conventional Cherenkov amplifiers that utilize the slow TM waveguide mode [2]–[10]. The CMA considered here interacts

Manuscript received 16 February 2022; revised 28 April 2022; accepted 29 May 2022. Date of publication 13 June 2022; date of current version 13 July 2022. This work was supported by Multidisciplinary University Research Initiative (MURI) (Exploration of Fundamental Limits to High Power Electromagnetic (HPEM) Amplification) through the Air Force Office of Scientific Research (AFOSR) under Grant FA9550-20-1-0409. The review of this article was arranged by Senior Editor J. G. Leopold. (Corresponding author: Paul Argyle.)

Paul Argyle was with the Department of Physics, Brigham Young University, Provo, UT 84602 USA. He is now with the Department of Physics, University of Maryland, College Park, MD 20742 USA (e-mail: paulargyle20@gmail.com).

Phillip Sprangle is with the Institute for Research in Electronics and Applied Physics, University of Maryland, College Park, MD 20742 USA.

Color versions of one or more figures in this article are available at https://doi.org/10.1109/TPS.2022.3180634.

Digital Object Identifier 10.1109/TPS.2022.3180634

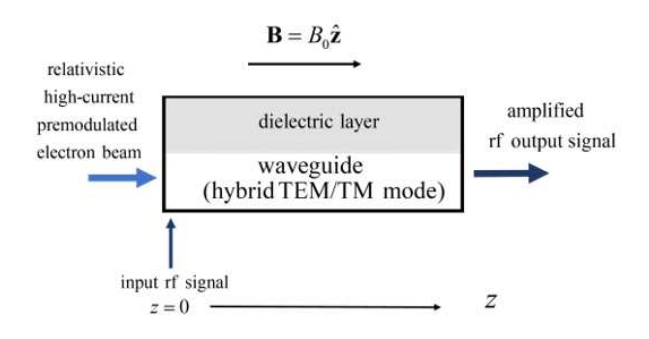


Fig. 1. Overall schematic of the CMA.

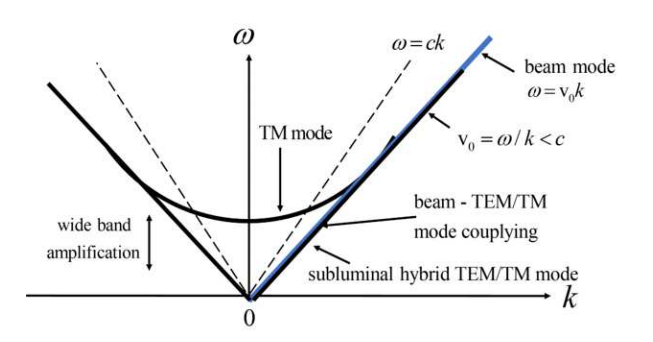
with a slow hybrid TEM waveguide mode [1]. An overall schematic of the CMA is shown in Fig. 1. The waveguide is lined with a dielectric material to reduce the phase velocity of the hybrid TEM/TM mode to equal the injected electron beam axial velocity. In this way, the injected electron beam can couple to the hybrid TEM/TM subluminal mode and amplify the input signal. A pure TE mode has a phase velocity equal to c and no axial electric field. There is a TM component to the hybrid mode since the mode has an axial electric field component. The dielectric liner introduces an axial field and velocity less than c. The extended frequency interaction region provides extremely wideband amplification capability.

The dispersion diagram, indicating the interaction between the hybrid TEM/TM subluminal waveguide mode and the beam mode, is shown in Fig. 2. The coupling between the electron beam mode and the slow TEM/TM waveguide mode takes place over a wide range of frequencies. The operating frequency is below the TM cutoff frequency. In this interaction, the ratio of the axial electric field (bunching field) to the transverse field, at resonance, is $|E_z|/|E_x| \sim 1/\gamma_0$. The relativistic factor is in the range $\gamma_0 \sim 2-3$, corresponding to electron beam energies of $\sim 0.5-1$ MeV. Excitation of the hybrid TEM/TM mode allows for coupling of the output radiation to a transmitting antenna, by tapering away the dielectric layer, and converting to a pure TEM mode. The efficiency of converting kinetic beam energy to radiation can be enhanced by spatially tapering the dielectric waveguide, i.e., phase velocity of the interacting wave, and/or by premodulating the beam current at the signal wavelength.

II. CMA MODEL

In the CMA, the electrons are restricted to move in the z-direction by application of a large axial magnetic field. The cross-sectional view of the CMA is shown in Fig. 3. The CMA is azimuthally symmetric, i.e., $\partial/\partial\varphi=0$ and the minor radius of the annular electron beam, Δr_B , is much less than the major radius, r_B . Since $\Delta r_B/r_B\ll 1$, the analysis can be performed in the Cartesian geometry.

0093-3813 © 2022 IEEE. Personal use is permitted, but republication/redistribution requires IEEE permission. See https://www.ieee.org/publications/rights/index.html for more information.



Dispersion diagram showing the coupling between subluminal hybrid TEM/TM and beam mode over a wide frequency range. Wideband amplification takes place below the cutoff frequency of the TM mode.

Axially symmetric fields, $\partial / \partial \varphi = 0$ Cross sectional cut of waveguide annular beam dielectric & conductor (a)

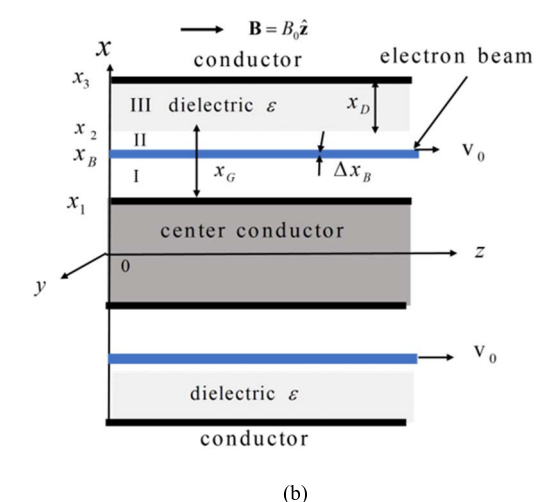


Fig. 3. (a) Cross-sectional views of the CMA configuration. The dielectric layer extends from $x = x_2$ to $x = x_3$ and $\Delta x_B \ll x_B$. (b) Cross-sectional view of CMA configuration in the Cartesian geometry.

III. CMA DISPERSION RELATION

The dispersion relation is derived in the thin beam limit $\Delta x_B \ll x_B$. The waveguide is divided into three regions consisting of vacuum gaps below and above the electron beam and the dielectric layer, as shown in Fig. 3(b). The axial electric field, responsible for modulating the electron beam, is given by

$$E_z(x, z, t) = \text{Re}[Eh(x)\exp(i(kz - \omega t))]$$
 (1)

where E is the complex amplitude, h(x) denotes the transverse profile, k is the complex wavenumber, and ω is the operating frequency. The wave equation governing the evolution of the axial field is $(\partial^2/\partial x^2 - c^{-2}\partial^2/\partial t^2)E_z = \mu_0(\partial J/\partial t + c^2\partial\rho/\partial z)$. In the linear regime, the current density and charge density are $J \to \delta J = i \varepsilon_0 \omega \xi_B E_z$ and $\rho \to \delta \rho = i \varepsilon_0 k \xi_B E_z$, respectively, where $\xi_B = (\omega_B^2/\gamma_0^3)(\omega - v_0 k)^{-2}$, $\omega_B = (q^2 n_B/m\varepsilon_0)^{1/2}$ is the beam plasma frequency, n_B is the beam density, $\gamma_0 =$ $(1-v_0^2/c^2)^{-1/2}$ is the relativistic mass factor, and v_0 is the axial electron velocity.

The full dispersion relation is derived in Appendix A by matching boundary conditions across all the regions shown in Fig. 3(b) and is given by

$$n^{2}k_{\perp}\tan(k_{\perp}x_{G}) + k_{\perp,D}\tan(k_{\perp,D}x_{D}) = -\xi_{B}G(k,\omega)H(k,\omega)$$
(2)

where

$$G(k,\omega) = k_{\perp} \Delta x_B \sin(k_{\perp}(x_B - x_1)) \frac{\cos(k_{\perp}(x_2 - x_B))}{\cos(k_{\perp}x_G)}$$
(3a)

$$H(k, \omega) = k_{\perp,D} \tan(k_{\perp,D} x_D) + n^2 k_{\perp} \tan(k_{\perp} (x_2 - x_B))$$
 (3b)

 $k_{\perp}=(\omega^2/c^2-k^2)^{1/2}$ is the transverse wavenumber in regions 1 and 2, $k_{\perp,D}=(n^2\omega^2/c^2-k^2)^{1/2}$ is the transverse wavenumber in region 3 (dielectric), $n = (\varepsilon/\varepsilon_0)^{1/2}$ is the index of refraction, ε is the dielectric constant of the dielectric liner, $x_G = x_2 - x_1$, and $x_D = x_3 - x_2$. The left-hand side of (2) represents the dielectric waveguide mode that is coupled to the beam modes, $\omega - v_0 k \approx 0$.

The dispersion relation in (2) can be simplified by approximating both sides in the vicinity of the beam mode, where $k \approx \omega/v_0$, so that $k_{\perp} \approx i \alpha_{\perp} \omega/c$ and $k_{\perp,D} \approx \alpha_{\perp,D} \omega/c$, where $\alpha_{\perp} = 1/(\beta_0 \gamma_0)$ and $\alpha_{\perp,D} = (n^2 \beta_0^2 - 1)^{1/2}/\beta_0$. Expanding the dielectric waveguide mode to third order in the tangent arguments and the right-hand side of (2) in the vicinity of the beam mode the dispersion relation reduces to

$$(k - k_{\text{TEM}}(\omega))(k - \omega/v_0)^2 = -K_B^3(\omega) \tag{4}$$

where

$$k_{\text{TEM}}(\omega) = \sqrt{1 + \chi(\omega)} \frac{\omega}{v_{\text{TEM}}}$$
 (5a)

$$\chi(\omega) = \frac{\left(\alpha_{\perp}^4 x_G^3 + \alpha_{\perp,D}^4 x_D^3 / n^2\right)}{3(x_G + x_D)} \frac{\omega^2}{c^2}$$
 (5b)

$$v_{\text{TEM}} = c \left(\frac{x_G + x_D/n^2}{x_G + x_D} \right)^{1/2}$$

$$K_B^3(\omega) = \frac{\omega_B^2/c^2}{2\gamma_0^5 \beta_0^3} \frac{\Delta x_B}{(x_G + x_D/n^2)}$$
(5c)

$$K_B^3(\omega) = \frac{\omega_B^2/c^2}{2\gamma_0^5 \beta_0^3} \frac{\Delta x_B}{(x_G + x_D/n^2)}$$

$$\times \left(\frac{\sinh(\alpha_{\perp}(x_B - x_1)\omega/c)}{\cosh(\alpha_{\perp}x_G\omega/c)}\right)^2 \frac{\omega}{c}.$$
 (5d)

The dispersion relation describes the coupling between the subluminal hybrid TEM/TM mode, $\omega \approx v_{\text{TEM}}k$, and the two beam modes, $\omega \approx v_0 k$. The wavenumber associated with the subluminal TEM-TM waveguide mode is $k_{\text{TEM}}(\omega)$ and the phase velocity of the hybrid TEM-TM wave is $v_{\rm ph}(\omega) =$ $\omega/k_{\text{TEM}}(\omega) = v_{\text{TEM}}/(1+\chi(\omega))^{1/2} < c$. Maximum coupling with the beam occurs when $v_{\text{TEM}} \approx v_0$. At resonance, the ratio of the axial electric field to the transverse field is $|E_z|/|E_x| = 1/\gamma_0$, where $\gamma_0 \approx 2-3$, indicating that a substantial fraction of the electromagnetic energy flux is in the axial direction.

A further simplification of the dispersion relation can be made so that the parameter dependence of the growth rates and wavenumber shifts can be seen explicitly. In the long-wavelength limit, the trigonometric functions in (2) are simplified by making a small argument approximation, i.e., $|k_{\perp}x_G| < 1$ and $|k_{\perp,D}x_D| < 1$. The dispersion relation in (2) near resonance, i.e., $\omega/k = v_{\text{TEM}} \approx v_0$, reduces to

$$(k - k_{\text{TEM}})(k - \omega/v_0)^2 = -f_0(\omega/c)^3$$
 (6)

where

$$f_0 = \frac{\omega_B^2}{2\gamma_0^7 \beta_0^5} \frac{\Delta x_B (x_B - x_1)^2}{x_G + x_D/n^2}.$$
 (7)

To obtain the spatial growth rate and wavenumber shift at resonance, i.e., $v_0 = v_{\rm TEM}$, we substitute $k = \omega/v_0 + \delta k$, where $|\delta k| \ll \omega/v_0$. The wavenumber shift and the spatial growth rate are $\delta k_R = Re(\delta k)$ and $\Gamma = -\delta k_I = -Im(\delta k)$, respectively. It is convenient to introduce the unitless Budker parameter, $v_B = (\omega_B^2/2c^2)r_B\Delta x_B = I_B/(I_C\beta_0)$, where r_B is the radius of the annular beam, I_B is the beam current in units of amperes, and $I_C = 4\pi m\varepsilon_0 c^3/q = 1.7 \times 10^4$ A. In terms of Budker's parameter, with r_B replaced by x_B , $f_0 = v_B \gamma_0^{-7} \beta_0^{-5} (x_B - x_1)^2 (x_B (x_G + x_D/n^2))^{-1}$ and the wavenumber shift and growth rate in the long-wavelength limit are given by

$$\delta k_R = (1/2) f_0^{1/3} \omega / c$$
 (8a)

$$\Gamma = \left(\sqrt{3}/2\right) f_0^{1/3} \omega/c. \tag{8b}$$

A. Conversion Efficiency Estimates Using Linear Theory

The conversion efficiency, in the absence of tapering and/or premodulating the beam, can be estimated using the linear wavenumber shift in (8a). The conversion efficiency is defined as

$$\eta = \frac{P_{\text{out}}}{V_B I_B} = \frac{\Delta \gamma}{\gamma_0 - 1} \tag{9}$$

where $P_{\rm out}$ is the output radiation power at saturation, $V_B = (\gamma_0 - 1)mc^2/q$ is the electron beam voltage, and $\Delta \gamma$ is the average change in γ at saturation. The change in γ at saturation can be estimated by assuming that at saturation, the average velocity of the trapped electrons is equal to the phase velocity of the trapping wave, $\omega/(k+\delta k_R)$, which is initially less than the beam velocity v_0 . The change in average beam velocity at saturation is therefore $\Delta v_{\rm sat} \approx v_0 \delta k_R/k$ and the change in γ is $\Delta \gamma \approx \beta_0 \gamma_0^3 \Delta v_{\rm sat}/c$. The conversion efficiency, using arguments from the linear theory, is $\eta_L \approx f_{\rm trap} \beta_0^2 \gamma_0^3 (\gamma_0 - 1)^{-1} \delta k_R/k$, and with the use of (8a), it is given by

$$\eta_L \approx \frac{f_{\text{trap}}}{2} \frac{\beta_0 \gamma_0^3}{(\gamma_0 - 1)} f_o^{1/3}$$
(10)

where $f_{\rm trap}$ is the fraction of electrons trapped, e.g., $f_{\rm trap} \sim 1$.

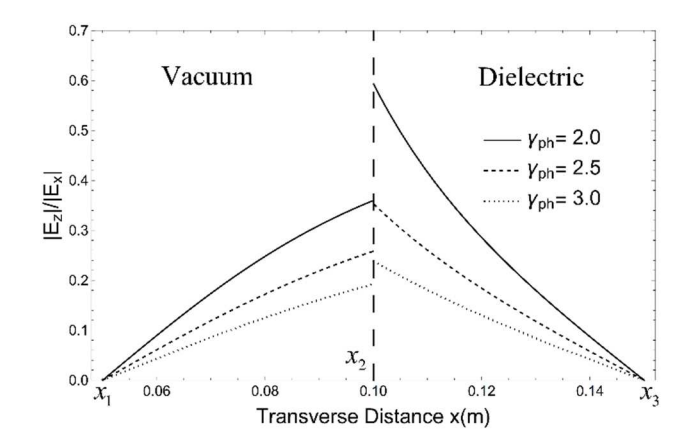


Fig. 4. Ratio of axial to transverse electric field within the waveguide for various values of γ_{ph} .

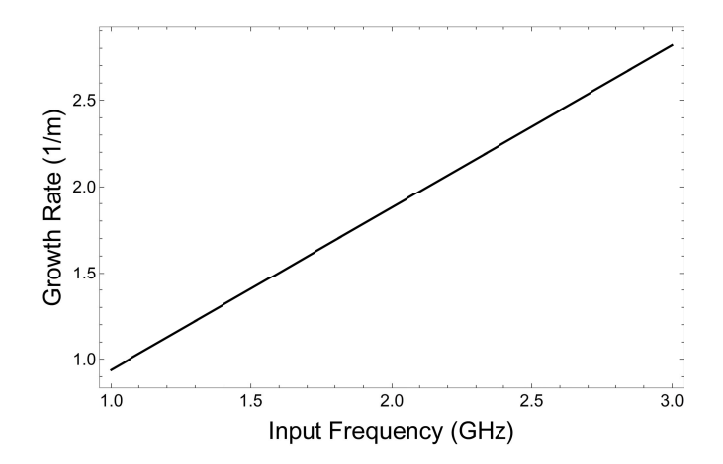


Fig. 5. Linear spatial growth rate (8b), as a function of frequency from f=1-3 GHz. The beam current is $I_B=5$ kA and the waveguide dimensions and dielectric constant of the dielectric layer are listed in Table I.

Fig. 4 shows the ratio of the magnitude of the axial field to the transverse field as a function of transverse distance within the dielectric loaded waveguide for various values $\gamma_{\rm ph} = \gamma_0$. The values correspond to electron beam energies, from $E_B = (\gamma_0 - 1)mc^2 = 0.5$ –1 MeV. Optimum coupling between the electron beam and the subliminal hybrid TEM/TM waveguide mode takes place when $\gamma_{\rm ph} = \gamma_0$. The field ratio scales as $|E_z|/|E_x| \sim 1/\gamma_0$, as pointed out earlier. The electron beam is located near the dielectric surface, $x = x_2$. The field ratio is obtained by solving for the fields together with the dispersion relation as described in Appendix A.

Fig. 5 shows the linear growth rate obtained from (6) for the parameters given in Table I. The signal e-folding length, $1/\Gamma$, ranges from ≈ 1 m at f = 1 GHz to ≈ 0.3 m at f = 3 GHz.

B. Estimate of Output Power

The output radiation power at saturation, using the efficiency in (10), is given by

$$P_{\text{out}} = \eta_L V_B I_B = 2.56 \times 10^5 f_{\text{trap}} \beta_0 \gamma_0^3 f_0^{1/3} I_B.$$
 (11)

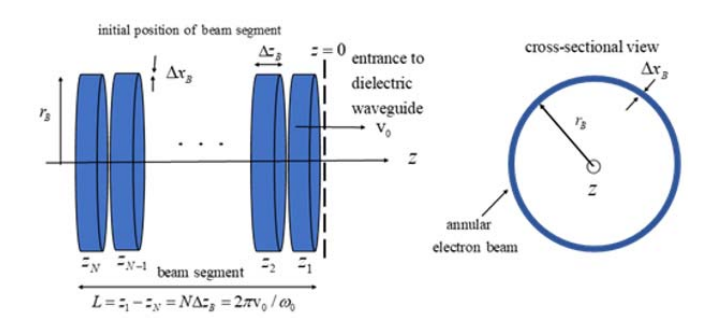


Fig. 6. Configuration and geometry of a beam segment of length L. The beam segment consists of $N = L/\Delta z_B$ subsegments that enter the dielectric waveguide at z = 0.

The radiation power scaling in (11) indicates that output powers in the gigawatt range can be generated by electron beams having energies and currents in the megaelectronvolt and multi-kiloampere range.

IV. NONLINEAR FORMULATION

The set of coupled, self-consistent equations for the spatial evolution of the field amplitude and phase, in terms of averages over the electron orbits, is described in detail in Appendix B. In formulating the nonlinear dynamics of the CMA, the system is assumed to be in the steady state such that the only time dependence is at the operating frequency ω_0 . In the steady state, the injected electron beam can be divided into segments of length $L=2\pi v_0/\omega_0$. The electrons in each segment undergo the same trajectory as the corresponding electron in any other segment, however, displaced in time by integers of $2\pi/\omega_0$. In the steady state, the fields vary in space, apart from the carrier frequency ω_0 .

In the simulations, the number of electrons in a beam segment is typically N = 100.

The beam segment L is divided into N subdivisions. These subdivisions are shown in Fig. 6 as rings with radial thickness Δx_B and length Δz_B . The electrons in a particular subdivision all undergo identical trajectories if Δz_B is sufficiently small. Therefore, a single electron can be assigned to a subsection having an enhanced charge equal to the actual number of electrons. The steady-state, nonlinear formulation is based on solving the wave equation for E_z consistent with the appropriate boundary conditions together with the electron orbit equations. The coupled set of equations is expressed in terms of the independent variable z.

The wave equation for the axial subluminal TEM/TM field is

$$\begin{split} \left(\partial^2/\partial x^2 + \partial^2/\partial z^2 - c^{-2}\partial^2/\partial t^2\right) E(x, z, t) \\ &= \mu_0 \left(\partial J/\partial t + c^2 \partial \rho/\partial z\right) \end{split}$$

where the charge and current densities are given by sums over individual electron orbits

$$\rho(x,z,t) = q \Delta z_B \Delta x_B n_B \sum_{i=1}^{N} g_i \delta(z - \tilde{z}_j(t)) \delta(x - x_B) \quad (12a)$$

$$J(x,z,t) = q \Delta z_B \Delta x_B n_B \sum_{j=1}^{N} g_j \tilde{v}_j(t) \delta(z - \tilde{z}_j(t)) \delta(x - x_B).$$
(12b)

The axial position of the jth electron is $\tilde{z}_j(z_{0j},t) = z_{0j} + v_0 t + \delta \tilde{z}_j(z_{0j},t)$ and $\tilde{v}_j(z_{0j},t) = \partial \tilde{z}_j(z_{0j},t)/\partial t = v_{0j} + \partial \delta \tilde{z}_j(z_{0j},t)/\partial t$ is the velocity of the jth electron and $N = (2\pi v_0/\omega_0)/\Delta z_B$ is the number of electrons in a beam segment. The injected electron beam velocities are assumed to be the same, i.e., $v_{0j} = v_0$, cold beam. The modulation factor $g_j(z_{0j})$ denotes the initial distribution of the injected electron density, e.g., for an unmodulated injected beam $g_j = 1$ and the average is $\langle g_j \rangle = N^{-1} \sum_{j=1}^N g_j = 1$.

In the nonlinear formulation, the phase velocity of the trapping wave can be spatially varied by tapering the wavenumber $k_{\text{TEM}}(z)$ associated with the dielectric waveguide. Tapering of the wavenumber is accomplished by spatially varying the parameters of the dielectric waveguide. In addition, the ability to premodulate the injected beam to enhance conversion efficiency is accomplished by appropriately modifying the factor g_j . Examples of tapering $k_{\text{TEM}}(z)$ and premodulating the beam to enhance efficiency are given in Section V.

The axial field experience by the *j*th electron is

$$E_z(x, z, z_{0j}) = \operatorname{Re}\left[A_0(z) \exp(i\Psi_j(z, z_{0,j}))\right]$$
(13)

where $A_0(z) = E_0(0) \exp(-\int_0^z \delta k_I(z'))dz')$ is the field amplitude and $\Psi_j(z,z_{0,j})$ is the phase with respect to the jth electron and $x=x_B$. The initial amplitude $E_0(0)$ is provided by the input signal to the CMA. The complex wavenumber of the field is $k(z) = k_0 + \delta k_R + i \delta k_I$. The phase of the jth electron is given by

$$\Psi_{j}(z) = \int_{0}^{z} \left(k_{0}(z') + \partial \theta(z') / \partial z' - \frac{\omega_{0}}{V_{i}(z')} \right) dz' + \Psi_{0j} \quad (14)$$

where $V_j(z, z_{0j})$ is the velocity of the jth electron at position z, which entered the interaction region with initial conditions, $(\Psi_j)_{z=0} = \Psi_{0j} = -\omega_0 z_{0j}/v_0$ and $(\partial \Psi_j/\partial z)_{z=0} = k_0(0) + \partial \theta(0)/\partial z - \omega_0/v_0$. Using the relativistic Lorentz force equation, the phase is shown in Appendix B-A to satisfy a generalized pendulum equation given by

$$\frac{\partial^2 \Psi_j(z)}{\partial z^2} = \frac{\partial k_0}{\partial z} + \frac{\partial^2 \theta}{\partial z^2} + \left(\frac{\omega_0}{c}\right)^2 \left(\frac{1}{\gamma_j} \frac{c}{V_j}\right)^3 \tilde{A}_0(z) \cos \Psi_j(z)$$
(15)

where $\tilde{A}_0(z) = q A_0(z)/(mc\omega_0)$ is the unitless normalized amplitude of the axial field.

The wave equation together with the sources in (12a) and (12b) is solved using Green's function method, which considers the boundary conditions across the interfaces in the dielectric waveguide. The result of this procedure, in Appendix B, is a set of coupled equations for the axial field amplitude and phase

$$2K_{S}\langle \tilde{S}(z)\rangle_{R} = \left(k_{0}^{2} - k_{\text{TEM}}^{2} + 2k_{0}\frac{\partial\theta}{\partial z} + \left(\frac{\partial\theta}{\partial z}\right)^{2}\right)\tilde{A}_{0}(z)$$
$$-\left(\Gamma^{2} + \frac{\partial\Gamma}{\partial z}\right)\tilde{A}_{0}(z) \tag{16a}$$

3.0

TABLE I	
PARAMETERS USED IN SIMULATIONS	

beam energy	$E_B = 0.74 \mathrm{MeV} (\gamma_0 = 2.5)$
average beam current	$I_B = 5 \text{ kA}$
Budker's parameter	$V_B = 0.31$
signal frequency	f = 1 - 3 GHz
signal wavelength	$\lambda_0 = 30 - 10 \mathrm{cm}$
input signal power	$P_{in} = 10 \mathrm{kW}$
dielectric constant	$\varepsilon = 1.47\varepsilon_0$
inner conductor radius	$x_1 = 0.05 \mathrm{m}$
beam major radius	$x_B = 0.085\mathrm{m}$
beam minor radius	$\Delta x_B = 0.01 \mathrm{m}$
inner radius of dielectric liner	$x_2 = 0.1 \mathrm{m}$
outer radius of dielectric liner	$x_3 = 0.15 \mathrm{m}$

$$\left(2k_0\Gamma + \frac{\partial k_0}{\partial z} + 2\Gamma \frac{\partial \theta}{\partial z} + \frac{\partial^2 \theta}{\partial z^2}\right) \tilde{A}_0(z)
= -2K_S \langle \tilde{S}(z) \rangle_I$$
(16b)

where $\Gamma(z) = -\delta k_I(z)$ is the growth rate and $\theta(z) = \int_0^z \delta k_R(z') dz'$ is the phase

$$\langle \tilde{S}(z) \rangle_{R} = \frac{\omega_{B}^{2}}{c^{2}} \Delta x_{B} \beta_{0} \left\langle \frac{g_{j}c^{2}}{\gamma_{j}^{2}V_{j}^{2}} \left(\sin \Psi_{j} - \frac{\gamma_{j}^{2}}{\omega_{0}} \frac{\partial V_{j}}{\partial z} \cos \Psi_{j} \right) \right\rangle_{\Psi_{0}}$$

$$(17a)$$

$$\langle \tilde{S}(z) \rangle_{I} = \frac{\omega_{B}^{2}}{c^{2}} \Delta x_{B} \beta_{0} \left\langle \frac{g_{j}c^{2}}{\gamma_{j}^{2}V_{j}^{2}} \left(\cos \Psi_{j} + \frac{\gamma_{j}^{2}}{\omega_{0}} \frac{\partial V_{j}}{\partial z} \sin \Psi_{j} \right) \right\rangle_{\Psi_{0}}$$

$$(17b)$$

$$V_j(z) = \omega_0/(k_0 + \delta k_R - \partial \Psi_j/\partial z)$$
 and $\langle \dots \rangle_{\psi_0} = (1/2\pi) \int_0^{2\pi} (\dots) d\Psi_{0j}$.

The set of coupled self-consistent nonlinear equations, (15), (16a), (16b), (17a), and (17b), is numerically solved.

V. CMA SIMULATIONS

The parameters used in the following simulations are given in Table I.

The coupled equations are solved in *Mathematica*. The implicit differential-algebraic solver, with a residual method for equation simplification, was used. Twelve-digit accuracy and precision goals were used for all simulations.

Fig. 7(a) shows the signal power as a function of distance. The signal frequency is f = 2 GHz and the unmodulated beam current is $I_B = 5$ kA. The input power was $P_{\rm in} = 10$ kW and the output power was $P_{\rm out} = 0.9$ GW at z = 3.2 m. The corresponding conversion efficiency versus distance is shown

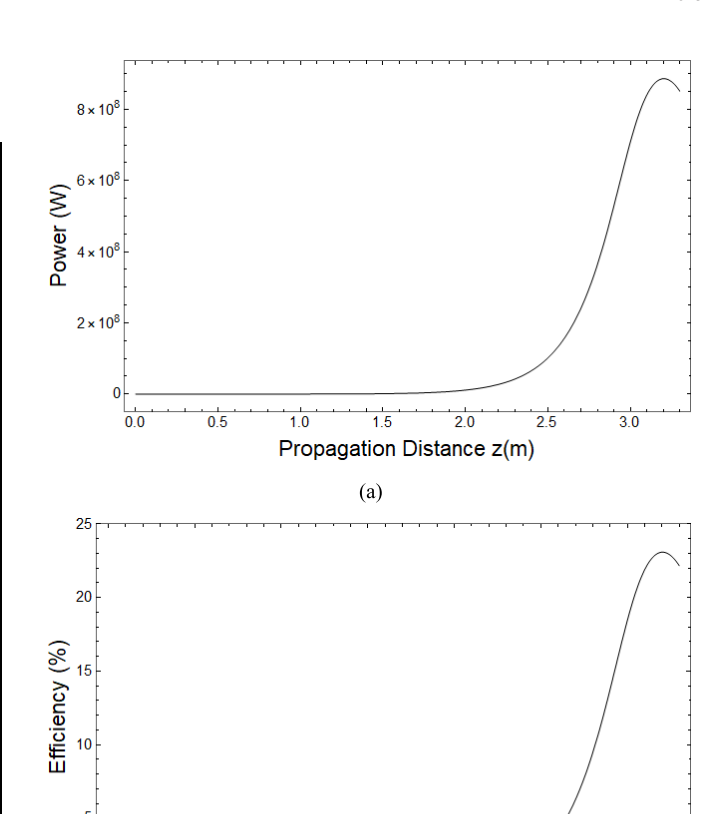


Fig. 7. (a) Radiation power versus distance. Maximum power, $P_{\rm out} = 0.9$ GW, is reached at a distance of 3.2 m. The signal frequency is 2 GHz and the electron beam is unmodulated. The parameters are given in Table I. (b) Conversion efficiency versus distance for the parameters used in (a). A maximum efficiency of 23% reached at a distance of 3.2 m. The number of beam subsegments was N = 100.

(b)

Propagation Distance z(m)

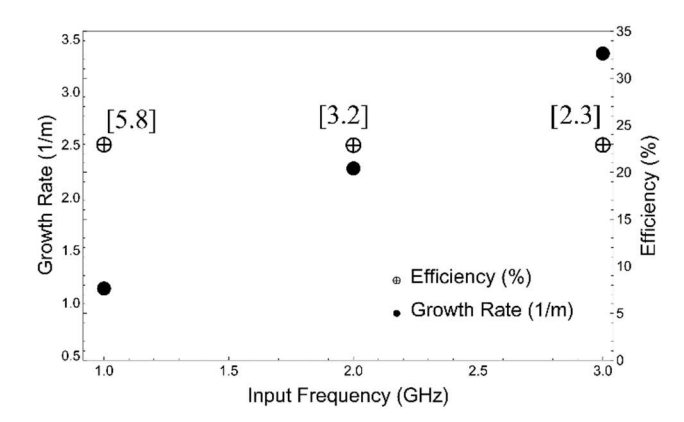


Fig. 8. Spatial growth rate and efficiency as a function of frequency over the range f=1-3 GHz. The beam current is $I_B=5$ kA and input power is $P_{\rm in}=10$ kW. The solid circles \bullet denote the growth rate and the circles \oplus denote the conversion efficiency. The numbers in brackets give the saturation distance in meters. The waveguide dimensions and dielectric constant of the dielectric layer are listed in Table I.

in Fig. 7(b) and reaches a maximum of $\eta = 23\%$. The number of electron beam subsegments was N = 100.

Fig. 8 shows the growth rate obtained from simulations in the linear (small-signal) regime and the corresponding conversion efficiency over a frequency range of f = 1-3 GHz.

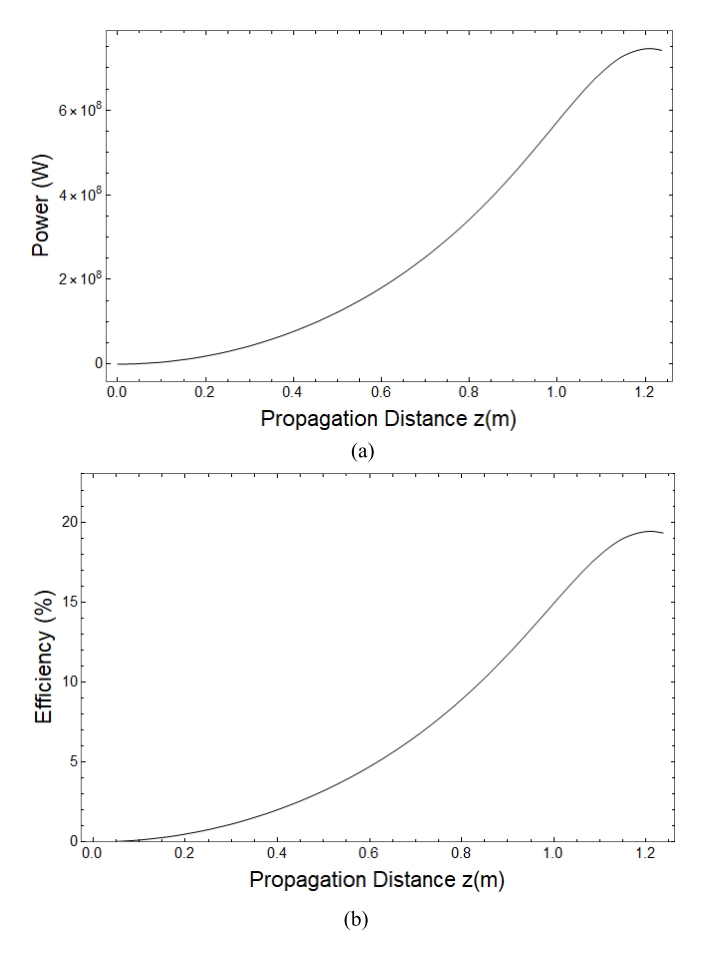


Fig. 9. (a) Radiation power versus distance. The maximum power of $P_{\rm out}=0.75$ GW is reached at a distance of 1.2 m. The signal frequency is 2 GHz and the electron beam is 50% premodulated (sinusoidally) at the signal wavelength, $\lambda_0=15$ cm (2 GHz). The parameters for this example are given in Table I. (b) Conversion efficiency versus distance for the parameters used in Fig. 7(a) and for a 50% premodulation (sinusoidally) beam. Maximum efficiency of 19% is reached at a distance of z=1.2 m. The number of beam subsegments was N=100.

The numbers in brackets denote the saturation distance in meters. The parameters used in these simulations are listed in Table I. The growth rates obtained from the simulations are approximately equal to the growth rates obtained from the dispersion relation (6). The small difference is due to the fact that in the simulations, the linear regime is not well defined. The e-folding length associated with the field is not much less than the interaction length, i.e., field saturation takes place over short distances.

A. Premodulated Beam

In the second example shown in Fig. 9(a) and (b), the parameters are the same as those used in Fig. 7(a) and (b), except that the electron beam is premodulated. Fig. 9(a) shows the radiation power as a function of distance. The signal frequency is f = 2 GHz and the average premodulated beam current is $I_B = 5$ kA. The input power is $P_{\rm in} = 10$ kW and the output power is $P_{\rm out} = 0.75$ GW at z = 1.2 m. The conversion efficiency versus distance is shown in Fig. 9(b) and reaches a maximum of $\eta = 19\%$.

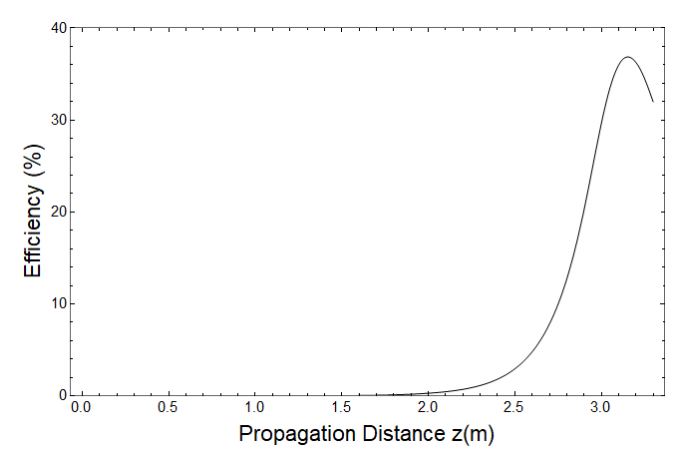


Fig. 10. Enhanced conversion efficiency versus distance for the parameters used in Fig. 7(a). The maximum efficiency of 37% is reached at a distance of z = 3.2 m. In this example, the waveguide wavenumber k_{TEM} is decreased by 5% beginning at z = 2.0 m. The number of beam subsegments was N = 100.

B. Tapered Dielectric Waveguide

Conversion efficiency can be enhanced by decreasing the phase velocity of the trapped electron just prior to saturation. This is accomplished by spatially tapering (increasing) the wavenumber k_{TEM} in (5a). An example of this enhancement method is shown in Fig. 10.

VI. SUMMARY AND DISCUSSION

The CMA is based on the interaction between the beam mode and the subluminal hybrid TEM/TM mode of a dielectrically lined waveguide. The mode is below the TM cutoff frequency and allows for amplification of an input signal over a wide frequency range. Excitation of the subliminal TEM/TM mode also allows for coupling the output radiation to a transmitting antenna, by tapering away the dielectric layer, and converting the mode to a pure TEM mode. In this interaction, the ratio of the axial electric field to the transverse field, at resonance, is $|E_z|/|E_x| \approx 1/\gamma_0$, where $\gamma_0 \sim 2-3$. The analysis and simulations have been performed in the linear regime and the nonlinear regimes. We show that conversion efficiencies can be enhanced by appropriately spatially tapering the dielectric waveguide and/or by premodulating the injected electron beam. Further improvement in efficiency can be achieved by the use of a depressed collector.

To restrict the beam trajectories to the axial direction, an axial magnetic field is necessary. The requirement on the magnetic field is that the cyclotron frequency is much greater than the plasma frequency, i.e., $\Omega_0 = q B_0/(\gamma_0 m) \gg \omega_B/\gamma_0^{3/2}$, and this requires that $B_0 \gg (m/q)\omega_B/\gamma_0^{1/2}$. For the parameters used in our examples, this inequality is well satisfied for magnetic fields of $B_0 \ge 1$ kG.

Electron beams in the tens of kiloamperes and multimegaelectronvolt regime are readily available [11]. These beams are generated from field emission cathodes and typically have a pulse duration in the tens of nanosecond regime and can be rep-rated. For the parameters used in our examples, the e-folding time, i.e., $(\Gamma v_0)^{-1}$, is typically a few nanoseconds. Therefore, the amplified signal will saturate during a single electron beam pulse duration.

The potential variation due to self-fields across the electron beam from $x = x_B \pm \Delta x_B$ introduces an effective velocity spread (shear). The fractional spread in electron energy due to self-field effects should be somewhat less than the cold beam conversion efficiency. The fractional energy spread due to self-fields is $\delta \gamma/(\gamma_0 - 1) = \nu_B(\Delta x_B/r_B)/(\gamma_0 - 1)$. For the parameters used in the simulations, $\delta \gamma/(\gamma_0 - 1) = \nu_B(\Delta x_B/r_B)/(\gamma_0 - 1) \approx 0.02\%$, which is far less than the conversion efficiencies.

In the following, some of the issues pertaining to the CMA based on the interaction between the beam and the subluminal TEM/TM mode are discussed. Charging of the dielectric by the beam's halo is a potential issue. In our examples, the outer edge of the beam is 1.0 cm from the dielectric. Application of a sufficiently large axial magnetic field would mitigate dielectric charging. Power levels on the order of gigawatts and multi-kiloampere electron beams can, of course, present challenging breakdown issues. Dielectric breakdown, due to the large radiation and self-space charge electric fields, must be avoided. Self-fields on the dielectric can be reduced by placing the dielectric layer on the inner wall, inside the annular beam, rather than outside the beam. Low loss ceramics, such as those in the magnesium-titanium oxide class, could provide an appropriate dielectric material for the CMA. It is planned that the 3-D, relativistic PIC code, Neptune [12], developed at the Naval Research Laboratory, will be used to further evaluate the CMA.

Typical parameters used in our simulation to generate gigawatt power levels in the 1–3-GHz range are: beam currents of \sim 5 kA and beam energies of \sim 1 MeV. Conversion efficiencies approaching 40% have been simulated by premodulating the electron beam and spatially tapering the waveguide over distances of a few meters. For input signal powers of 10 kW, saturation occurs at distances of less than a few meters at output powers greater than a gigawatt.

APPENDIX A

Here, the linear dispersion relation for the CMA interaction is obtained. The geometry of the CMA is shown in Fig. 3(a) and (b). The dispersion relation is derived in the limit of a thin electron beam, i.e., $\Delta x_B \ll x_G$, x_D , where $x_G = x_2 - x_1$ and $x_D = x_3 - x_1$. The procedure involves matching boundary conditions across regions I–III. The electron beam density is assumed to be uniform and confined to the region $x \leq x_B \pm \Delta x_B/2$ by a large axial magnetic field.

The axial electric field in region I $(x_1 \le x \le x_B - \Delta x_B/2)$

$$E_z(x, z, t) = \text{Re}[A\sin(k_{\perp}(x - x_1))\exp(i\varphi(z, t))]. \quad (A.1)$$

The axial electric field in region II $(x_B + \Delta x_B/2 \le x \le x_2)$ is

$$E_z(x, z, t) = \text{Re} \left[B \sin(k_{\perp}(x - x_B)) \exp(i\varphi(z, t)) + C \cos(k_{\perp}(x - x_B)) \exp(i\varphi(z, t)) \right]. \quad (A.2)$$

The axial electric field in region III $(x_2 < x < x_3)$ is

$$E_z(x, z, t) = \text{Re} \left[D \sin(k_{\perp, D}(x - x_3)) \exp(i\varphi(z, t)) \right]. \quad (A.3a)$$

In (A1)–(A3), A, B, C, and D are constant coefficients, $k_{\perp}^2 = \omega^2/c^2 - k^2$, $k_{\perp,D}^2 = n^2\omega^2/c^2 - k^2$, and $\varphi(z,t) = kz - \omega t$. The E_x - and B_y -fields in regions I and II are

$$E_x = i \frac{k}{k_\perp^2} \frac{\partial E_z}{\partial x} \tag{A.4a}$$

$$B_{y} = \frac{i\omega}{c^{2}k_{\perp}^{2}} \frac{\partial E_{z}}{\partial x}.$$
 (A.4b)

The E_x - and B_y -fields in region III are

$$E_x = i \frac{k}{k_{\perp,D}^2} \frac{\partial E_z}{\partial x}$$
 (A.5a)

$$B_{y} = \frac{i\omega}{c^{2}k_{\perp,D}^{2}} \frac{\varepsilon}{\varepsilon_{0}} \frac{\partial E_{z}}{\partial x}.$$
 (A.5b)

To match the magnetic field boundary condition across the thin electron beam located at $x=x_B$, the electron beam current density in terms of the axial electric field is needed. The perturbed beam current density is $\delta J=q(\delta nv_0+n_B\delta v)$, where δn and δv are the perturbed density and axial velocity to first order in the E_z field, respectively. The perturbed velocity and density are given, respectively, by the relativistic Lorentz force and continuity equation, $(\partial/\partial t+v_0\partial/\partial z)\delta v=(q/m)\gamma_0^{-3}E_z$ and $(\partial/\partial t+v_0\partial/\partial z)\delta n+n_B\partial\delta v/\partial z=0$, where E_z is the axial electric field given in (A1). The electron beam current density and the surface charge density are $\delta J=i\varepsilon_0\omega\xi_BE_z$ and $\delta\sigma=q\delta n\Delta x_B=i\varepsilon_0k\xi_B\Delta x_BE_z$, where $\xi_B=(\omega_B^2/\gamma_0^3)(\omega-v_0k)^{-2}$, $\gamma_0=(1-v_0^2/c^2)^{-1/2}$, and $\omega_B=(q^2n_B/m\varepsilon_0)^{1/2}$ is the beam plasma frequency.

The tangential component of the magnetic field across the electron beam is discontinuous by the surface current density. Equivalently, the normal component of the electric field is discontinuous across the electron beam by the surface charge density. Applying either boundary condition gives

$$B = A(k_{\perp}\xi_{B}\Delta x_{B}\sin(k_{\perp}(x_{B} - x_{1})) + \cos(k_{\perp}(x_{B} - x_{1}))).$$
(A.6)

Continuity of the tangential component of electric field across the beam, at $x = x_B$, and across the vacuum–dielectric interface, at $x = x_2$, gives, respectively

$$A\sin(k_{\perp}(x_B - x_1)) = C$$
 (A.7a)

$$B\sin(k_{\perp}(x_2 - x_B)) + C\cos(k_{\perp}(x_2 - x_B)) = -D\sin(k_{\perp}, p_1 x_D).$$

$$3\sin(k_{\perp}(x_2 - x_B)) + C\cos(k_{\perp}(x_2 - x_B)) = -D\sin(k_{\perp,D}x_D).$$
(A.7b)

Finally, applying the condition that the tangential component of magnetic field across the vacuum–dielectric interface is continuous yields

$$n^{2}k_{\perp}D\cos(k_{\perp,D}x_{D}) = k_{D,\perp}B\cos(k_{\perp}(x_{2} - x_{B})) - k_{D,\perp}C\sin(k_{\perp}(x_{2} - x_{B})).$$
 (A.8)

Eliminating the coefficients, A, B, C, and D in (A6)–(A8) yield the full dispersion relation in (2).

APPENDIX B

Here, the nonlinear steady-state formulation of the CMA is derived. In formulating the dynamics of the CMA, the system is assumed to be in the steady state such that the time dependence is at the operating frequency ω_0 . The steady-state, nonlinear formulation is based on solving self-consistently, the wave equation for E_z together with the electron orbit equations. The coupled set of equations is expressed in terms of the independent variable z. In the steady state, the fields vary along the axial position and oscillate at the wave frequency ω_0 .

The appendix is divided into two parts. In Appendix B-A, the source term driving the subluminal TEM/TM field, i.e., the electron beam's current density and charge density, is expressed in terms of the electron's relativistic nonlinear trajectories. A generalized pendulum equation is derived, which describes the nonlinear relativistic electron dynamics. In Appendix B-B, the nonlinear spatial evolution of the subluminal TEM/TM field, driven by the current and charge density, is derived. Here, the nonlinear evolution of the field amplitude and phase are self-consistently obtained by solving the wave equation together with the appropriate boundary conditions across the various interfaces in the dielectrically lined waveguide. Finally, the results from Appendixes B-A and B-B are combined to give a set of equations that selfconsistently describe the steady-state spatial evolution of the fields.

A. Driving Source for the Fields

In formulating the nonlinear dynamics of the CMA, the system is assumed to be in the steady state such that the only time dependence is at the operating frequency ω_0 . In the steady state, the fields vary along the axial position and oscillate at the wave frequency ω_0 . In the steady state, the injected electron beam can be divided into axial segments of length $L = 2\pi v_0/\omega_0$. The electrons in each segment undergo the same trajectory as the corresponding electrons in any other segment, however, displaced in time by integers of the wave period $2\pi/\omega_0$. Therefore, it is necessary to keep track of only those electrons in a beam segment of length $L = 2\pi v_0/\omega_0$. The beam segment L is further divided into N subdivisions of length Δz_B (see Fig. 6). In the thin beam limit, Δx_B is small, and the electrons in a particular subdivision Δz_B all undergo identical trajectories. In the present model, the injected electron beam velocities are taken to be equal, i.e., $v_{0i} = v_0$, cold beam.

The governing equation for the subluminal TEM/TM field is the wave equation

$$\left(\frac{\partial^2}{\partial x^2} + \frac{\partial^2}{\partial z^2} - \frac{1}{c^2} \frac{\partial^2}{\partial t^2}\right) E(x, z, t) = S(x, z, t)$$
 (B1)

where $S(x,z,t) = \mu_0(\partial J/\partial t + c^2 \partial \rho/\partial z)$ and J and ρ are the current and charge densities induced by E, respectively. The charge and current density of the electron beam are given by sums over electron orbits

$$\rho(x, z, t) = q \Delta z_B \Delta x_B n_B \sum_{j=1}^{N} g_j \delta(z - \tilde{z}_j(t)) \delta(x - x_B)$$
 (B2a)

$$J(x,z,t) = q \Delta z_B \Delta x_B n_B \sum_{j=1}^{N} g_j \tilde{v}_j(t) \delta(z - \tilde{z}_j(t)) \delta(x - x_B)$$
(B2b)

where $\tilde{z}_i(z_{0i},t) = z_{0i} + v_0 t + \delta \tilde{z}_i(z_{0i},t)$ is the axial trajectory of the jth electron in the subluminal TEM/TM mode, $\tilde{v}_i(z_{0i},t) = v_0 + \partial \delta \tilde{z}_i(z_{0i},t)/\partial t$ is the velocity of the jth electron, $N = (2\pi v_0/\omega_0) \Delta z_B$ is the number of electrons in a beam segment, and the modulation parameter $g_i(z_{0i})$ denotes the initial distribution of the injected electrons, e.g., for an unmodulated beam, $g_j = 1$. The average value of the modulation parameters is unity, i.e., $N^{-1} \sum_{j=1}^{N} g_j = 1$. The average is over electrons within a beam segment and $N = L/\Delta z_B = 2\pi v_0/(\Delta z_B \omega_0)$ is the number of electrons in a beam segment. By premodulating the electron beam, the conversion efficiency can be significantly enhanced. Efficiency enhancement can also be achieved by spatially tapering the phase velocity, $\omega_0/k_0(z)$, of the axial field when electrons are deeply trapped. The wavenumber $k_0(z)$ can be varied by tapering the dimensions of the waveguide or dielectric liner. Simulation examples of tapering and premodulating the electron beam to enhance efficiency are given in Section V.

The source term driving the axial field [see (B1)] is

$$S(x, z, t) = q \Delta z_B \Delta x_B n_B \mu_0 \sum_{j=1}^{N} g_j$$

$$\times \left(\frac{\partial}{\partial t} \left(\tilde{v}_j(t) \delta \left(z - \tilde{z}_j(t) \right) \right) + c^2 \frac{\partial}{\partial z} \delta \left(z - \tilde{z}_j(t) \right) \right) \delta(x - x_B). \quad (B3)$$

It is convenient to transform from the independent variable t to the independent variable z, i.e., steady-state regime. We first replace $\delta(z - \tilde{z}_i(z_{0j}, t))$, in (B2a) and (B2b), with

$$\delta(z - \tilde{z}_j(z_{0j}, t)) = \delta(t - \tau_j(z, z_{0j})) \left| \frac{\partial \tau_j}{\partial z} \right| = \frac{\delta(t - \tau_j(z, z_{0j}))}{|V_j(z, z_{0j})|}$$
(B4)

where

$$\tau_j(z, z_{0j}) = \int_0^z \frac{dz'}{V_j(z', z_{0j})} + \frac{z_{0j}}{v_0}.$$
 (B5)

In (B4), $\tau_j(z, z_{0j})$ and $V_j(z, z_{0j})$ represent the time and velocity of the *j*th electron at position *z* that entered the interaction region, z = 0 plane, at time $t_{0j} = z_{0j}/v_0$, respectively. Transforming the independent variables in the source term from *t* to *z* gives

$$S(x, z, t) = q \Delta z_B \Delta x_B n_B \mu_0 \sum_{j=1}^{N} g_j$$

$$\times \left(\frac{\partial}{\partial t} \delta(t - \tau_j(z)) + c^2 \frac{\partial}{\partial z} \right)$$

$$\times \left(\delta(t - \tau_j(z)) / |V_j(z)| \right) \delta(x - x_B) \quad (B6)$$

where we used the relations $\delta(z-\tilde{z}_j(t)) = \delta(t-\tau_j(z))/|V_j(z)|$ and $\tilde{v}_j(t) = \tilde{v}_j(\tau_j(z)) \equiv V_j(z)$.

Integrating the source term in (B6) over a wave period and across the thin electron beam gives $\langle S(z) \rangle = (\omega_0/2\pi) \int_0^{2\pi/\omega_0} dt \int_{x_B-\Delta x_B/2}^{x_B+\Delta x_B/2} dx S(x,z,t) \exp(-i\phi(z,t)),$ where

$$\langle S(z) \rangle = q \, \Delta z_B \, \Delta x_B \frac{n_B}{\varepsilon_0} \frac{\omega_0}{2\pi} \sum_{j=1}^N g_j$$

$$\times \left(-i \frac{\omega_0}{c^2} \exp(i\omega_0 \tau_j(z)) + \frac{\partial}{\partial z} \left(\frac{\exp(i\omega_0 \tau_j(z))}{|V_j(z)|} \right) \right)$$

$$\times \exp\left(-i \int_0^z k_R(z') dz' \right). \tag{B7}$$

It is convenient to express the orbit equations in terms of the phase $\Psi_j(z, z_{0j}) = \phi(z, \tau_j(z)) + \int_0^z \delta k_R(z') dz'$ of the *j*th electron with respect to the axial electric field. The phase of the *j*th electron is given by

$$\Psi_{j}(z, z_{0j}) = \int_{0}^{z} \left(k_{0}(z') + \delta k_{R}(z') - \frac{\omega_{0}}{V_{j}(z', z_{0j})} \right) dz' + \Psi_{0j}$$
(B8)

where the initial conditions are $(\Psi_j)_{z=0} = \Psi_{0j} = -\omega_0 z_{0j}/v_0$ and $(\partial \Psi_j/\partial z)_{z=0} = k_0(0) + \delta k_R(0) - \omega_0/v_0$. Writing (B7) in terms of the phase Ψ_j gives

$$\langle S(z) \rangle = \frac{q n_B}{\varepsilon_0} \Delta x_B v_0 \left\langle \frac{g_j}{\gamma_j^2 V_j^2} \left(i \omega_0 - \gamma_j^2 \frac{\partial V_j}{\partial z} \right) \exp(-i \Psi_j) \right\rangle_{\Psi_0}$$
(B9)

where the sum over individual electrons is replaced with an average over the phases and $\langle \ldots \rangle_{\Psi_0} = (1/2\pi) \int_0^{2\pi} (\ldots) d\Psi_{0j}$.

The equation of motion governing the phase Ψ_j can be put into the form of a generalized pendulum equation. The axial velocity of the jth electron in the time domain is given by the relativistic orbit equation, $\partial \tilde{v}_j(z_{0j},t)/\partial t=(q/m)\tilde{v}_j^{-3}E_z(x_B,\tilde{z}_j(z_{0j},t),t)$, where $E_z(x_B,z,t)=\text{Re}[E_0(0)\exp(i\int_0^z\delta k(z')dz')\exp(i\phi(z,t))],$ $\phi(z,t)=\int_0^zk_0(z')dz'-\omega_0t,\ \delta k(z)=\delta k_R+i\delta k_I,\ \text{and}$ $\tilde{v}_j(z)=(1-(\tilde{v}_j/c)^2)^{-1/2}.$ In the steady state, the relativistic orbit equation is $V_j\partial V_j/\partial z=(q/m)v_j^{-3}E_z(x_B,z,\tau_j(z,z_{0j})),$ where $\tau_j(z,z_{0j})$ is given by (B5)

$$E_z(x_B, z, \tau_j) = \text{Re}\left[E_0(0) \exp\left(i \int_0^z k(z') dz'\right) \exp\left(-i\omega_0 \tau_j\right)\right]$$

= \text{Re}\[A_0(z) \exp(i \Psi_j(z, z_{0,j}))\]

and $k(z) = k_0 + \delta k_R + i \, \delta k_I$. The orbit equation of the *j*th electron is $V_j \partial V_j / \partial z = (q/2m) \gamma_j^{-3}(z) A_0(z) \exp(i \Psi_j(z, z_{0,j}) + c.c.)$, where $A_0(z) = E_0(0) \exp(-\int_0^z \delta k_I(z')) dz'$ is the field amplitude and $\gamma_j(z) = (1 - (V_j/c)^2)^{-1/2}$. The orbit equation can be written in the form of a generalized pendulum equation

$$\frac{\partial^2 \Psi_j(z)}{\partial z^2} = \frac{\partial k_0}{\partial z} + \frac{\partial \delta k_R}{\partial z} + \frac{q}{m} \frac{\omega_0}{V_j^3(z) \gamma_j^3(z)} A_0(z) \cos \Psi_j(z)$$
(B10)

where we used the relations, $\partial V_j/\partial z = V_j^2(\partial^2 \Psi_j/\partial z^2 - \partial k_0/\partial z - \partial \delta k_R/\partial z)/\omega_0$ and $V_j(z) = \omega_0/(k_0 + \delta k_R - \partial \Psi_j/\partial z)$.

B. Boundary Conditions

In this section, the evolution of the TEM/TM electric fields is obtained in terms of the electron trajectories as described by the generalized pendulum equation in (B10). The following procedure involves solving the wave equation (B1) together with the appropriate boundary conditions within the dielectric waveguide. This is essentially an application of Green's function method. This procedure results in a set of self-consistent equations for the field amplitude and phase in terms of the electron trajectories.

In the steady state, the CMA operates at a single frequency ω_0 . Multiplying both sides of (B1) by $\exp(i\omega_0 t)$ and integrating over a wave period, 0 to $2\pi/\omega_0$, give $(\partial^2/\partial x^2 + \partial^2/\partial z^2 + \omega_0^2/c^2)E_z(x,z) = S_0(x,z)$, where $E(x,z,t) = \text{Re}[E_z(x,z)\exp(-i\omega_0 t)]$ and

$$S_0(x,z) = \frac{\omega_0}{2\pi} \int_0^{2\pi/\omega_0} dt S(x,z,t) \exp(i\omega_0 t).$$
 (B11)

Taking the Fourier transform in z gives $(\partial^2/\partial x^2 + k_\perp^2)\hat{E}_z(x,\kappa) = \hat{S}_0(x,\kappa)$, where $k_\perp = (\omega_0^2/c^2 - \kappa^2)^{1/2}$, $\hat{E}_z(x,\kappa) = (2\pi)^{-1/2}\int_{-\infty}^{\infty} E_z(x,z)\exp(-i\kappa z)dz$, and $\hat{S}_0(x,\kappa) = (2\pi)^{-1/2}\int_{-\infty}^{\infty} S_0(x,z)\exp(-i\kappa z)dz$. Integrating across the beam, from $x_B - \varepsilon$ to $x_B + \varepsilon$, gives $\partial \hat{E}_z/\partial x|_{x=x_B+\varepsilon} - \partial \hat{E}_z/\partial x|_{x=x_B-\varepsilon} = \hat{S}_0(x_B,\kappa)$, where $\varepsilon \to 0$. In Appendix A, the Fourier representation of E_z in region I $(x_1 < x < x_B)$ and region II $(x_B < x < x_2)$ is $\hat{E}_z(x,\kappa) = A\sin(k_\perp(x-x_1))$ and $\hat{E}_z(x,\kappa) = B\sin(k_\perp(x-x_B)) + C\cos(k_\perp(x-x_B))$, respectively. Using the E_z -field representations in (A1) and (A2), we find that $\partial \hat{E}_z/\partial x|_{x=x_B+\varepsilon} - \partial \hat{E}_z/\partial x|_{x=x_B-\varepsilon} = k_\perp B - k_\perp A\cos(k_\perp(x_B-x_1))$. The transformed wave equation evaluated at the location of the beam $x=x_B$ is

$$\left(\frac{B}{A} - \cos(k_{\perp}(x_B - x_1))\right) \frac{k_{\perp} \hat{E}_z(x_B, \kappa)}{\sin(k_{\perp}(x_B - x_1))} = \hat{S}_0(x_B, \kappa)$$
(B12)

where $\hat{E}_z(x_B, \kappa) = A \sin(k_\perp(x_B - x_1))$. The ratio B/A is obtained by applying boundary conditions across x_B and x_2 [see (A7a), (A7b), and (A8)]. Applying the boundary conditions and making the small argument, long-wavelength approximation, we obtain

$$\frac{B}{A} = -\frac{n^2 k_\perp^2 (x_B - x_1)}{k_{D,\perp}^2 x_D + n^2 k_\perp^2 (x_2 - x_B)}.$$
 (B13)

Substituting (B13) into (B12)

$$\left(\kappa^2 - k_{\text{TEM}}^2\right) \hat{E}_z(x_B, \kappa) = K_S \hat{S}_0(x_B, \kappa) \tag{B14}$$

where $f_S = (x_B - x_1)^2 (x_G + x_D/n^2)^{-1} k_{\text{TEM}}^2 / \gamma_{\text{TEM}}^2$, $k_{\text{TEM}}^2 = (x_D + x_G)(x_G + x_D/n^2)\omega_0^2/c^2$, and $\gamma_{\text{TEM}} = n((x_G + x_D)/(n^2 - 1)x_D)^{1/2} \approx \gamma_0$ near resonance. Taking the inverse Fourier transform of (B14) gives the equation for the spatial evolution of the field

$$\left(\frac{\partial^2}{\partial z^2} + k_{\text{TEM}}^2\right) E_z(x_B, z) = -f_S S_0(x_B, z).$$
 (B15)

The axial field is represented by

$$E_z(x_B, z) = \text{Re}\left[E_0(0) \exp\left(i \int_0^z k(z')dz'\right)\right]$$

= Re
$$\left[A_0(z) \exp(i\theta(z)) \exp\left(i \int_0^z k_0(z') dz'\right) \right]$$
(B16)

where $A_0(z) = E_0(0) \exp(\int_0^z \Gamma(z')dz')$ is the amplitude, $\Gamma(z) = -\delta k_I(z)$ is the growth rate, and $\theta(z) = \int_0^z \delta k_R(z')dz'$ is the phase. Substituting (B16) into (B15) and multiplying both sides by $\exp(-i \int_0^z (k_0 + \delta k_R)dz')$ give

$$2f_S\langle S(z)\rangle = \left((k_0 + \delta k_R)^2 - \delta k_I^2 + \frac{\partial k_I}{\partial z} - k_{\text{TEM}}^2 \right) A_0(z) + i \left(2\delta k_I (k_0 + \delta k_R) - \frac{\partial (k_0 + \delta k_R)}{\partial z} \right) A_0(z).$$
(B17)

where $\langle S(z) \rangle = \int_{x_B - \varepsilon}^{x_B - \varepsilon} S_0(x, z) dx \exp(-i \int_0^z (k_0 + \delta k_R) dz')$ and $k = k_0 + \delta k_R + i \delta k_I$.

To complete the nonlinear CMA formulation, the source term $\langle S(z) \rangle$ in (B9) is substituted into the reduced wave equation (B17). Equating real and imaginary terms gives the final set of self-consistent nonlinear equations (16a) and (16b) together with (17a) and (17b).

ACKNOWLEDGMENT

The authors would like to thank Thomas Antonsen for the useful suggestions.

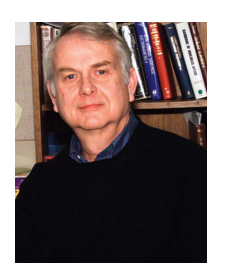
REFERENCES

- P. Argyle, T. Antonsen, and P. Sprangle, "Cherenkov maser amplifier, nonlinear analysis and simulations," in *Proc. IEEE 23rd Conf. Vac. Electron.*, Monterey, CA, USA, Apa. 2022, pp. 85–87.
- [2] D. Shiffler, J. Luginsland, D. M. French, and J. Watrous, "A Cerenkov-like maser based on a metamaterial structure," *IEEE Trans. Plasma Sci.*, vol. 38, no. 6, pp. 1462–1465, Jun. 2010.
 [3] P. Jeffrey and A. M. Cook, "Design and large-signal modeling of a
- [3] P. Jeffrey and A. M. Cook, "Design and large-signal modeling of a W-band dielectric TWT," *IEEE Trans. Plasma Sci.*, vol. 45, no. 10, pp. 2820–2834, Sep. 2017.
- [4] W. Main, R. Cherry, and E. Garate, "200 MW S-band dielectric Cherenkov maser oscillator," Appl. Phys. Lett., vol. 55, no. 15, pp. 1498–1500, Oct. 1989.
- [5] W. Peter, E. Garate, W. Main, and A. Fisher, "High-gain X-band dielectric Cherenkov maser," *Phys. Rev. Lett.*, vol. 65, no. 24, pp. 2989–2992, Dec. 1990.

- [6] H. Kosai, E. P. Garate, A. Fisher, and W. T. Main, "X-band dielectric cerenkov maser amplifier experiment," *IEEE Trans. Plasma Sci.*, vol. 20, no. 3, pp. 288–292, Jun. 1992.
- [7] W. Peter and E. Garate, "Stimulated Cherenkov emission in dielectric-lined waveguides," *Phys. Rev. A, Gen. Phys.*, vol. 45, no. 12, pp. 8833–8841, Jun. 1992.
- [8] A. S. Shlapakovskii and K. A. Chirko, "Dielectric Cherenkov masers as powerful amplifiers with superwide bandwidth," *IEEE Trans. Plasma Sci.*, vol. 22, no. 5, pp. 544–546, Oct. 1994.
- [9] J.-S. Choi, E.-G. Heo, B.-H. Hong, and D.-I. Choi, "Nonlinear saturation characteristics of a dielectric Cherenkov maser," *Nucl. Instrum. Methods Phys. Res. A, Accel. Spectrom. Detect. Assoc. Equip.*, vol. 375, nos. 1–3, pp. 175–178, Jun. 1996.
- [10] S. E. Tsimring, Electron Beams and Microwave Vacuum Electronics. Hoboken, NJ, USA: Wiley, 2006.
- [11] S. J. Cooke et al., "Vacuum electronic device design using 3D EM-PIC," in Proc. IEEE Int. Vac. Electron. Conf., Monterey, CA, USA, Apr. 2014, pp. 1–10.



Paul Argyle (Member, IEEE) received the bachelor's degree in physics from Brigham Young University, Provo, UT, USA, in 2022. He is currently pursuing the Ph.D. degree in physics with the University of Maryland, College Park, MD, USA, with research interest in nonlinear optics.



Phillip Sprangle (Life Fellow, IEEE) is currently a Professor of electrical and computer engineering and physics with the University of Maryland, College Park, MD, USA, and an Emeritus Scientist at the U.S. Naval Research Laboratory, Washington, DC, USA. He has published over 300 refereed articles and holds 20 U.S. patents. His research covers a wide range of fields, including the propagation and generation of high-energy lasers, laser-driven accelerators, ultrashort pulse laser-matter interaction, nonlinear optics, and free-electron lasers.

Prof. Sprangle is a fellow of Optical Society of America (OSA), American Physical Society (APS), and Directed Energy Professional Society (DEPS). He received the Presidential Rank Award, the Advanced Accelerator Concept Prize, the James Clerk Maxwell Prize, the Fred E. Saalfeld Award, the Navy Meritorious Civilian Service Award, the IEEE Plasma Science Award, the Sigma Xi Pure Science Award, the International Free Electron Laser Prize, the E. O. Hulburt Science and Engineering Award, and the Top Navy Scientist and Engineer of the Year Award.